PHYSICAL REVIEW APPLIED **14,** 034065 (2020)

Quantum-Enhanced Fiber-Optic Gyroscopes Using Quadrature Squeezing and Continuous-Variable Entanglement

Michael R. Grace,[1,*] Christos N. Gagatsos,[1] Quntao Zhuang,[1,2] and Saikat Guha[1]

[1] *James C. Wyant College of Optical Sciences, University of Arizona, Tucson, Arizona 85721, USA*
[2] *Department of Electrical and Computer Engineering, University of Arizona, Tucson, Arizona 85721, USA*

(Received 22 April 2020; revised 26 June 2020; accepted 7 July 2020; published 25 September 2020)

We evaluate the fundamental performance of a fiber-optic gyroscope (FOG) design that is enhanced by the injection of a quantum-optical squeezed vacuum. In the presence of fiber loss, we compute the optimum attainable enhancement below the standard quantum limit in terms of the angular velocity estimator variance from a homodyne measurement. We find that currently realizable amounts of single-mode squeezing are sufficient to access the maximum quantitative improvement, but that this gain in maximum rotation sensitivity is limited to a marginal constant factor. We then propose an entanglement-enhanced FOG design that segments a fixed amount of available fiber into multiple fiber interferometers and feeds this sensor array with a multimode-entangled squeezed vacuum resource. Our design raises the fundamental improvement in sensitivity to an appreciable factor of $e \approx 2.718$.

DOI: 10.1103/PhysRevApplied.14.034065

I. INTRODUCTION

Quantum-enhanced sensing [1–3] is a rapidly growing field and one of the tangible near-future quantum technologies. In the domain of optical sensing, quantum-enhanced systems utilize nonclassical states of light and/or nonclassical optical detection schemes to improve the quantifiable performance of various sensing tasks. Among these nonclassical optical effects, squeezing and entanglement are two key backbones that are known to produce major performance enhancements in many emerging optical sensing applications [4–11].

Quadrature-squeezed light is a well-established nonclassical resource dating to pioneering works of Caves, Shapiro, Yuen, and others [12–15]. Squeezing refers to a controllable phenomenon where quantum uncertainty is allocated asymmetrically between two noncommuting observables (e.g., the orthogonal quadratures of the complex field amplitude for an optical mode), while obeying the fundamental uncertainty relationship that lower bounds the product of their variances [16,17]. Squeezed vacuum (SV) states of light can be generated using spontaneous parametric down-conversion (SPDC), and experimental squeezing capability is steadily improving: vacuum states with quantum noise reduction of 10–15 decibels (dB) in a given quadrature has been achieved in recent years [18,19]. Quadrature squeezing is now routinely utilized in physical experiments relating to quantum information and sensing, most notably in the famous Laser Interferometer Gravitational-Wave Observatory (LIGO) [4,5].

On the other hand, quantum entanglement, i.e., correlations that are stronger than and cannot be described by classical probability theory, is still being explored for enhancement of optical sensing systems. Recent theoretical and experimental works have established that entanglement can enable superior precision for quantitative sensing tasks, including target detection [6,7], positioning [8], digital memory readout [9,10], and magnetometry [11].

More recently, entanglement has been shown to give an advantage in measuring global features of a signal using a sensor network, a topic termed “distributed quantum sensing” [20–27]. One such idea is a continuous-variable (CV) distributed quantum sensing protocol [20,28] that generates a multimode entangled optical probe by a splitting single-mode squeezed vacuum using a passive beam splitter network. CV distributed quantum sensing, which has been experimentally validated [29,30], is especially attractive from the experimental standpoint due to robustness against optical losses. The core idea in Ref. [20] has led to applications such as optical beam-displacement tracking [31] and quantum-enhanced machine learning for optical sensor–based signal classification [32] and has potential for other sensing contexts.

The fiber-optic gyroscope (FOG) is a high precision, compact solution for precision navigation in GPS-denied environments, ultraprecise platform stabilization, and other inertial sensing applications [33]. FOGs leverage the Sagnac principle [34], i.e., that light traveling along one branch of a rotating interferometer will undergo a

---

[*] michaelgrace@email.arizona.edu

detectable phase shift with respect to the light in the other branch. With kilometers of fiber needed for high sensitivity, fiber loss is a significant factor in FOG performance. Recent developments for FOGs include hollow core fiber coils [35], integrated optical sources and homodyne detectors, and laser-driven FOGs that bypass the conventional requirement for temporally incoherent sources [36,37]. In addition, quantum enhancement has recently been considered to boost rotation sensitivity [38–45], and preliminary experimental works on quantum-enhanced FOGs have demonstrated improvements via injection of squeezed vacuum states [39] and entangled NOON states [43].

In this paper, we first establish the fundamental sensitivity achievable by the squeezing-enhanced FOG design proposed in Ref. [39], for which a single-mode SV is injected to boost sensitivity. Our quantifying figure of merit for sensitivity is the estimator variance from sensing a small rotation. Then, inspired by recent theoretical work on distributed quantum sensing [20–22], we propose and analyze the fundamental performance of a CV entanglement-enhanced FOG design that uses a stacked array of multiple identical interferometers, where one part of an entangled optical state is distributed to each.

The main results of our investigation are the following.

(a) **Squeezing-enhanced FOG.** In Sec. II we analyze a classical FOG (termed *design C*), i.e., a fiber Sagnac interferometer read by a laser, as a baseline sensor design (Fig. 2). In Sec. III we calculate the rotation sensitivity achievable with the *squeezing-enhanced FOG* (*design S*) reported in Ref. [39]. Ignoring losses, design S achieves a Heisenberg-limited scaling advantage in sensitivity [1–3]; with fiber loss, the quantum advantage falls to a constant factor that depends on the amount of squeezing. Optimizing design S over the fiber length, we find that squeezing beyond 10–15 dB yields diminishing returns in sensitivity (Fig. 3), so currently existing technology could access the quantum advantage. However, in Sec. V we show that design S provides at best a small improvement factor of 1.196 over an optimized design C, capping its practical potential.

(b) **CV entanglement-enhanced FOG.** In Sec. IV we propose a *CV entanglement-enhanced FOG* (*design E*), in which a single-mode SV is split into an M-mode entangled state and injected into M parallel fiber interferometers (Fig. 4). We compare its sensitivity to that of a *product-state squeezing-enhanced FOG* (*design P*), which is equivalent to M parallel copies of design S, each with an independent squeezer, and a baseline *distributed classical FOG* (*design D*), which is M independent copies of design C. Assuming a constant dB/km of fiber loss, we evaluate these designs in two contexts.

(i) *Unconstrained total fiber length*. With optimized total fiber lengths, design P improves upon design D in sensitivity under a per-fiber power constraint, but it uses M single-mode squeezers to do so. Our resource-efficient design E leverages both distributed sensing and quantum sensing to achieve this same performance with just a single squeezer, requiring the generation of M-fold less squeezed energy (Fig. 5). Design E surpasses design S in sensitivity by a factor of M, mirroring the M-fold improvement of design D over design C. Still, in Sec. V we show that the improvement of design E over an optimized design D is again limited to 1.196.

(ii) *Constrained total fiber length*. If the total fiber length is held fixed under a weight or payload requirement, design E again outperforms designs D and P when M is optimized for each (Fig. 6). Unlike with an unconstrained fiber length, design E attains a notable sensitivity improvement over design D that is independent of both the fiber loss (dB/km) and the total fiber length. We find in Sec. V a maximum improvement factor of $e \approx 2.718$ in the limit of infinite squeezing (Fig. 8). Most of this benefit is attainable with 10–15 dB of squeezing, so our design E could provide an appreciable real-world sensitivity enhancement in the near future.

II. CLASSICAL FOG

A. Sagnac interferometry

A Sagnac interferometer measures angular velocity via the optical path delay induced in counterpropagating paths around a rotating loop (Fig. 1). For a laser-driven FOG, the resulting relative phase shift is given by [46]

$$\Delta\phi = \frac{4\omega m\vec{A}\cdot\vec{\Omega}}{c^2}, \tag{1}$$

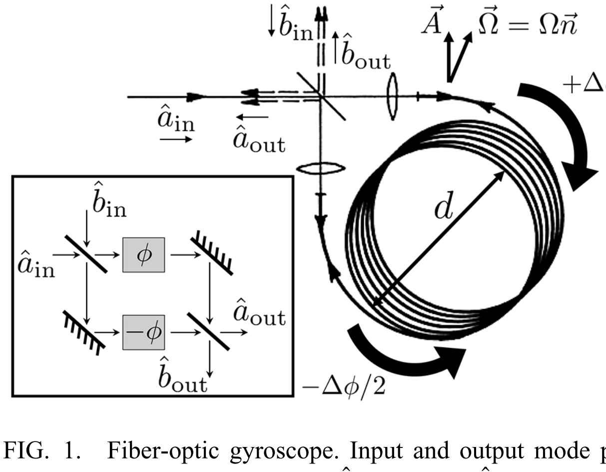

FIG. 1. Fiber-optic gyroscope. Input and output mode pairs, identified by field operators $\hat{a}_{\text{in}}$, $\hat{b}_{\text{in}}$, $\hat{a}_{\text{out}}$, and $\hat{b}_{\text{out}}$, are spatially colocated at the external ports of the coupling beam splitter. Adapted from Ref. [33]. Inset: Mach-Zehnder interferometer with conjugate phases $\pm\phi$. The input and output modes can be conceptually mapped to those of the FOG.

where ω is the optical center frequency of the laser, m is the number of fiber loops in the coil, $\vec{A}$ is the directed area of a single fiber loop, $\vec{\Omega} = \Omega\vec{n}$ is the directed angular velocity of rotation with magnitude $\Omega \in \mathbb{R}$ and unit-norm direction vector $\vec{n}$, and c is the speed of light in a vacuum. If l is the fiber length of a circular coil and d is its diameter, then the integer number of fiber loops in the coil $m \equiv l/(\pi d)$ linearly scales the total effective area of the gyroscope. "The indices of refraction of the core and the cladding, the phase or group velocities, the dispersion of the medium or of the waveguide have no influence" on the nonreciprocal phase delay accumulated by the counterpropagating beams [46]. Equation (1) is valid to first order in $d\Omega/c$, corresponding to the standard regime of slow rotations compared with the speed of light [34].

In a realistic FOG system, the principal source of optical loss is the transmission loss accumulated over the length of the fiber due to scattering from imperfections and/or evanescent coupling. We use η to denote the effective transmissivity of each branch around the Sagnac interferometer. For a fiber with a length of l km, this transmissivity is given by $\eta = 10^{-bl/10}$, where b is a wavelength-dependent fiber loss coefficient with a typical value of $b \approx 0.5$ dB loss per km at 1550 nm.

B. Conjugate phase sensing with quantum optics

A Sagnac interferometer can be conceptually equated to a phase conjugate Mach-Zehnder interferometer (MZI) where $\pm\phi \equiv \pm\Delta\phi/2$ are the conjugate phases accumulated on the two optical paths due to the physical rotation of the sensor (Fig. 1 inset). In a FOG setup, the two input ports and the two output ports of the conceptual Mach-Zehnder interferometer are spatially overlapped on a single beam splitter (Fig. 1) and can be separated using a Faraday rotator, for example [39]. In quantum terminology, we define $(\hat{a}_{\text{in}}, \hat{a}_{\text{out}})$ and $(\hat{b}_{\text{in}}, \hat{b}_{\text{out}})$ as pairs of quantum field (annihilation) operators of spatially overlapping optical modes with opposite propagation directions (Fig. 1).

A homodyne measurement can be used to estimate the conjugate phase ϕ and subsequently the angular velocity $\Omega = 2\phi/T$, with scale factor $T \equiv 4\omega l(\vec{A}\cdot\vec{n})/(\pi d c^2)$. In Appendix A we derive the measurement statistics obtained by a quantum-noise-limited homodyne measurement performed along the imaginary quadrature of mode $\hat{b}_{\text{out}}$. Letting $\tilde{b}_{\text{out}}$ designate the output random variable from such a homodyne measurement, the mean of $\tilde{b}_{\text{out}}$ is

$$\begin{aligned}\langle\tilde{b}_{\text{out}}\rangle &= \langle\text{Im}(\hat{b}_{\text{out}})\rangle \\ &= \sqrt{\eta}[\sin(\phi)\langle\text{Re}(\hat{a}_{\text{in}})\rangle - \cos(\phi)\langle\text{Im}(\hat{b}_{\text{in}})\rangle] \end{aligned} \tag{2}$$

and its variance is

$$\begin{aligned}\langle\Delta\tilde{b}^2_{\text{out}}\rangle &= \langle\Delta\text{Im}(\hat{b}_{\text{out}})^2\rangle \\ &= \eta[\sin(\phi)^2\langle\Delta\text{Re}(\hat{a}_{\text{in}})^2\rangle + \cos(\phi)^2\langle\Delta\text{Im}(\hat{b}_{\text{in}})^2\rangle] \\ &\quad + \frac{1-\eta}{4}. \end{aligned} \tag{3}$$

For a given FOG modality, we identify an unbiased estimator with a mean equal to the true angular velocity Ω. The estimator variance will depend on $\langle\tilde{b}_{\text{out}}\rangle$ and $\langle\Delta\tilde{b}^2_{\text{out}}\rangle$, where the expectation values of the corresponding quantum field operators are taken over the quantum states $|\psi_a\rangle$ and $|\psi_b\rangle$ injected at the two input ports.

C. Classical FOG sensitivity

In a conventional laser-driven FOG setup (design C), the conceptual input mode $\hat{a}_{\text{in}}$ is fed with a laser, while mode $\hat{b}_{\text{in}}$ is physically overlapped by the output mode $\hat{b}_{\text{out}}$ and has no input [Fig. 2(a)]. The joint input across the two ports can be modeled using the two-mode quantum state $|\psi_a\rangle|\psi_b\rangle = |\alpha\rangle|0\rangle$, a tensor product between a coherent state with mean photon number $N_v \equiv \langle\psi_a|\hat{a}^\dagger_{\text{in}}\hat{a}_{\text{in}}|\psi_a\rangle = \alpha^2$ and a vacuum state ($\alpha \in \mathbb{R}$ without loss of generality). In the small rotation regime ($\phi \ll 1$), the homodyne measurement statistics become

$$\begin{aligned}\langle\tilde{b}_{\text{out}}\rangle &= \sqrt{\eta}[\sin(\phi)\alpha - \cos(\phi)\,0] \approx \phi\sqrt{\eta}\alpha, \\ \langle\Delta\tilde{b}^2_{\text{out}}\rangle &= \frac{\eta}{4}[\sin(\phi)^2 + \cos(\phi)^2] + \frac{1-\eta}{4} = \frac{1}{4}. \end{aligned} \tag{4}$$

Note that the mean is scaled by $\sqrt{\eta}$ while the variance arises from quantum noise and does not depend on loss. Thus, $\tilde{\Omega}_{\text{C}} = 2\tilde{b}_{\text{out}}/(T\sqrt{\eta}\alpha)$ is an unbiased estimator of the unknown parameter Ω. The sensitivity to rotation is

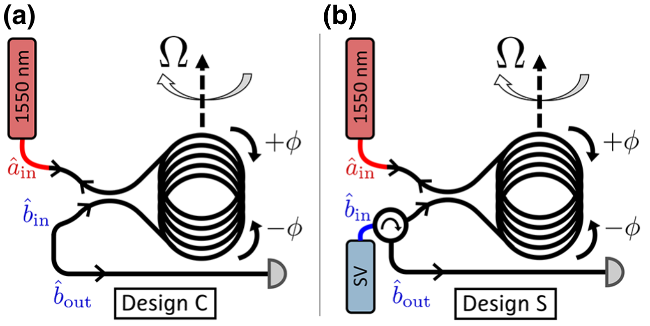

FIG. 2. (a) Classical FOG (design C) with coherent state in the $\hat{a}_{\text{in}}$ mode and vacuum in the $\hat{b}_{\text{in}}$ mode followed by homodyne detection of the $\hat{b}_{\text{out}}$ mode. (b) Squeezing-enhanced FOG (design S) with a single-mode SV injected at mode $\hat{b}_{\text{in}}$. The $\hat{b}_{\text{out}}$ mode is coupled to the homodyne detector using a Faraday rotator [39]. The local oscillators used for homodyning are not shown.

quantified by the estimator variance

$$\langle \Delta \tilde{\Omega}_{\mathrm{C}}^2 \rangle \approx \frac{1}{T^2 \eta \alpha^2} = \frac{1}{T^2 \eta N_v}. \tag{5}$$

This so-called standard quantum limit (SQL), which sets the best possible estimator variance for any sensor using purely classical probes and detectors, is characterized by inverse scaling with the total probe energy $N = N_v$. In terms of the fiber loss parameter b and the total fiber length $L = l$ used in the FOG, the estimator variance is

$$\langle \Delta \tilde{\Omega}_{\mathrm{C}}^2 \rangle \approx \frac{1}{V^{-2} N_v} \frac{1}{L^2 10^{-bL/10}}, \tag{6}$$

where we define $V \equiv l/T = \pi d c^2 / [4\omega(\vec{A} \cdot \vec{n})]$ to clarify the dependence of the FOG sensitivity on fiber length.

III. SQUEEZING-ENHANCED FOG

In this section, we compare the sensitivity attained by classical and squeezing-enhanced FOGs as a function of input energy. The squeezing-enhanced FOG utilizes a single-mode SV, for which squeezing is typically quantified in decibels of quantum noise reduction in the squeezed observable with respect to a vacuum. The squeezing parameter r and mean photon number N_s of an ideal single-mode SV state are related to σ, the amount of squeezing in units of decibels, by $r = \sigma \ln(10)/20$ and $N_s = \sinh^2[\sigma \ln(10)/20]$ [12,17].

A. Squeezing-enhanced FOG sensitivity

A simplified squeezing-enhanced FOG design (design S) is shown in Fig. 2(b), which is functionally equivalent to the design demonstrated in Ref. [39]. The vacuum input of design C is replaced by a vacuum that is squeezed along its imaginary quadrature, i.e., $|\psi_b\rangle = |0; -r\rangle$, $r \geq 0$, where the mean photon number of the SV state is given by $N_s = \langle \psi_b | \hat{b}_{\mathrm{in}}^{\dagger} \hat{b}_{\mathrm{in}} | \psi_b \rangle = \sinh^2(r)$ [12]. Considering the same ideal homodyne measurement as in design C in the presence of loss and in the $\phi \ll 1$ regime,

$$\begin{aligned} \langle \tilde{b}_{\mathrm{out}} \rangle &= \sqrt{\eta}[\sin(\phi)\alpha - \cos(\phi)\, 0] \approx \phi \sqrt{\eta} \alpha, \\ \langle \Delta \tilde{b}_{\mathrm{out}}^2 \rangle &= \frac{\eta}{4}[\sin(\phi)^2 + \cos(\phi)^2 e^{-2r}] + \frac{1-\eta}{4} \\ &\approx \frac{\eta e^{-2r} + 1 - \eta}{4}. \end{aligned} \tag{7}$$

In terms of the photon-unit probe energies N_v and N_s, the unbiased estimator $\tilde{\Omega}_{\mathrm{S}} = 2\tilde{b}_{\mathrm{out}}/(T\sqrt{\eta}\alpha)$ has variance

$$\begin{aligned} \langle \Delta \tilde{\Omega}_{\mathrm{S}}^2 \rangle &\approx \frac{\eta e^{-2r} + 1 - \eta}{T^2 \eta \alpha^2} \\ &= \frac{1}{T^2 \eta N_v} \left(\frac{\eta}{(\sqrt{1 + N_s} + \sqrt{N_s})^2} + 1 - \eta \right). \end{aligned} \tag{8}$$

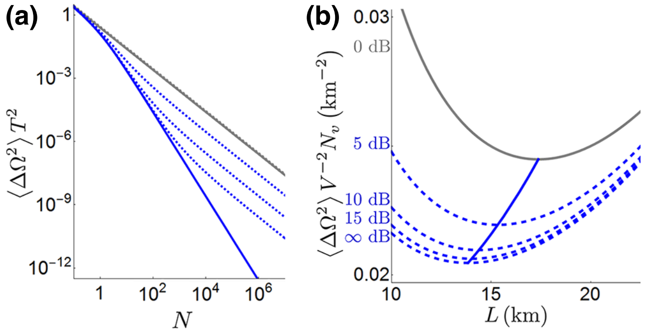

FIG. 3. (a) Normalized estimator variance for design C (gray) and design S (blue) for different fiber transmissivities η. Without loss, design S exhibits Heisenberg limited scaling, whereas loss results a constant-factor improvement compared with the SQL. Solid lines indicate $\eta = 1$. Dotted lines from top to bottom indicate $\eta = 0.9$, $\eta = 0.99$, and $\eta = 0.999$. (b) Fiber length dependence of the FOG rotation estimator variance with independent laser power and squeezing constraints, and with $b = 0.5$ km/dB of fiber loss. Gray line indicates design C. Blue dashed lines from top to bottom indicate design S with 5 dB squeezing, 10, 15, ∞ dB. The descending solid blue parametric curve indicates the design S estimator variance with optimized fiber lengths as the squeezing is increased.

If the total input mean photon number $N = N_v + N_s$ is constrained, the probe energy can be allocated between the laser and the SV to minimize the estimator variance. After some algebra, this minimum variance is found as

$$\langle \Delta \tilde{\Omega}_{\mathrm{S}}^2 \rangle |_{N_s = N_{s,\mathrm{opt}}} \approx \frac{2(1-\eta)^2}{T^2 \eta [1 + 2(1-\eta)N - z]}, \tag{9}$$

where $z = \sqrt{1 + 4\eta(1-\eta)N}$, and the corresponding SV mean photon number is $N_{s,\mathrm{opt}} = 2\eta^2 N^2 / [1 + z + 2\eta N(2 - \eta + z)]$. In the absence of loss, i.e., $\eta = 1$, the minimized estimator variance becomes $\lim_{\eta \to 1} \{ \langle \Delta \tilde{\Omega}_{\mathrm{S}}^2 \rangle |_{N_s = N_{s,\mathrm{opt}}} \} = 1/[T^2 N(N+1)]$. This inverse quadratic scaling with input energy, known as the Heisenberg limit (e.g., $\langle \Delta \tilde{\Omega}_{\mathrm{S}}^2 \rangle \propto 1/N^2$), is a fundamental improvement over SQL scaling and is a unique advantage of quantum-enhanced sensing [1–3]. In Fig. 3(a) we show the difference in scaling with input energy between the classical and squeezing-enhanced FOGs if loss is ignored. However, in the realistic case where $\eta < 1$, Heisenberg scaling is lost; for high input energy, the minimized estimator variance limits to $\lim_{N \to \infty} \{ \langle \Delta \tilde{\Omega}_{\mathrm{S}}^2 \rangle |_{N_s = N_{s,\mathrm{opt}}} \} = (1-\eta)/(T^2 \eta N)$. In this case, inverse scaling with probe energy is retained for design S (i.e., $\langle \Delta \tilde{\Omega}_{\mathrm{S}}^2 \rangle \propto \langle \Delta \tilde{\Omega}_{\mathrm{C}}^2 \rangle \propto 1/N$), yielding a constant factor improvement over the SQL of design C [Fig. 3(a)].

A more appropriate approach to the optimization of design S is to independently constrain N_v, the mean photon number from the laser, and N_s, the mean photon number of the injected SV. This distinction accounts for the fact that in practice squeezed light is more challenging or energy inefficient to produce than classical laser light, such that energy in a squeezed vacuum state is regarded as more "expensive" than energy in a coherent state. A full analysis constraining the total "wallplug" power required to pump the SPDC and the laser would be insightful but is not included here.

For a lossless ($\eta = 1$) squeezing-enhanced FOG in the high squeezing regime ($N_s \gg 1$, or $\sigma \gg 7.66$ dB), the rotation estimator variance [Eq. (8)] scales inversely with the product of the mean photon numbers from the two optical inputs (i.e., $\langle \Delta\tilde{\Omega}_\mathrm{S}^2 \rangle \propto 1/N_v N_s$), an alternative formulation of the Heisenberg limit. As before, optical loss restores SQL scaling (i.e., $\langle \Delta\tilde{\Omega}_\mathrm{S}^2 \rangle \propto \langle \Delta\tilde{\Omega}_\mathrm{C}^2 \rangle \propto 1/N_v$), resulting in a constant factor sensitivity improvement over the SQL for a given N_s. We quantify this improvement using the sensitivity ratio $R_\mathrm{S} = \langle \Delta\tilde{\Omega}_\mathrm{S}^2 \rangle / \langle \Delta\tilde{\Omega}_\mathrm{C}^2 \rangle$, where a smaller ratio means a greater improvement in quantum-enhanced performance over the SQL. The best achievable constant factor improvement for a given transmissivity η occurs with infinite squeezing and is easily calculated to be $\lim_{N_s \to \infty}\{R_\mathrm{S}\} = 1 - \eta$.

B. Squeezing-enhanced FOG sensitivity with optimized fiber length

In Fig. 3(b), we plot the estimator variances for designs C and S to compare their performance as a function of fiber length. Applying the fiber loss model with $l = L$, the estimator variance for design S [Eq. (8)] becomes

$$\langle \Delta\tilde{\Omega}_\mathrm{S}^2 \rangle \approx \frac{1}{V^{-2} N_v} \frac{1}{L^2 10^{-bL/10}} \times \left(\frac{10^{-bL/10}}{(\sqrt{1+N_s} + \sqrt{N_s})^2} + 1 - 10^{-bL/10} \right). \tag{10}$$

The relative performance gap can apparently be widened simply by cutting the total fiber length to suppress loss. However, this lowers the effective area of the interferometer [Eq. (1)], reducing absolute sensitivity to rotation.

Because of this balance and the convexity of $\langle \Delta\tilde{\Omega}_\mathrm{C}^2 \rangle$ and $\langle \Delta\tilde{\Omega}_\mathrm{S}^2 \rangle$, it is possible to find optimal total fiber lengths that minimize the estimator variances for designs C and S when there is no prior constraint on L. FOGs are often designed with shorter total fiber length than the optimal value in order to boost the dynamic range in angular velocity and to reduce the size and weight of the device [33]. Still, the optimal fiber length will yield the best possible sensitivity to small rotations, a desirable feature of a quantum-enhanced FOG.

To minimize the estimator variance for design C [Eq. (6)], we solve $\partial\langle \Delta\tilde{\Omega}_\mathrm{C}^2 \rangle / \partial L = 0$ and find the solution

$$L_\mathrm{opt} = \frac{20}{\ln(10) b} \approx \frac{8.686}{b}, \tag{11}$$

which is the fiber length known to optimize the signal-to-noise ratio of a classical FOG given a dB/km loss specification of b [33]. Assuming that $b = 0.5$ dB/km at 1550 nm, $L_\mathrm{opt} \approx 17.372$ km. The optimized estimator variance is

$$\langle \Delta\tilde{\Omega}_\mathrm{C}^2 \rangle|_{L=L_\mathrm{opt}} = \frac{1}{V^{-2} N_v} \frac{e^2 \ln(10)^2 b^2}{400}. \tag{12}$$

For the minimized estimator variance of design S [Eq. (10)], solving $\partial\langle \Delta\tilde{\Omega}_\mathrm{S}^2 \rangle / \partial L = 0$ yields the solution

$$L_\mathrm{opt} = \frac{10[2 + \Lambda(N_s)]}{\ln(10) b}, \tag{13}$$

where

$$\Lambda(x) = W\left(\frac{4[x - \sqrt{x(1+x)}]}{e^2} \right) \tag{14}$$

and $W(y)$ is the principal value of the Lambert W function. This corresponds to a minimized variance of

$$\langle \Delta\tilde{\Omega}_\mathrm{S}^2 \rangle|_{L=L_\mathrm{opt}} = \frac{1}{V^{-2} N_v} \frac{e^{2+\Lambda(N_s)} \ln(10)^2 b^2}{200[2 + \Lambda(N_s)]}. \tag{15}$$

The parametric curve in Fig. 3(b) shows that SV injection boosts the optimal FOG sensitivity while reducing the length of the fiber needed for a desired performance. For example, while a classical FOG achieves its optimal estimator variance with 17.37 km of 0.5 dB/km fiber, a 10.24 km FOG with 5 dB of squeezing exhibits the same sensitivity with more dynamic range and a lower payload. Furthermore, experimentally feasible single-mode squeezing (10–15 dB) achieves nearly the full constant-factor quantum advantage; more squeezing yields diminishing returns. This indicates that a fully realized squeezing-enhanced FOG is a near term attainable technology.

IV. ENTANGLEMENT-ENHANCED FOG

In this section we consider distributed sensing, where multiple identical Sagnac interferometers are simultaneously employed in parallel orientations on a single spool to measure the same physical rotation. Using M to denote the number of fiber-optic interferometers being used, the fiber length allocated to each interferometer becomes $l = L/M$, so $V = L/(MT)$. For distributed FOGs, it may be appropriate to constrain not the total mean photon number N_v of the laser light, but the *per-mode* mean photon number $n_v = N_v/M$, or, equivalently, a per-mode laser power constraint, to account for the peak power permitted by an optical fiber before the onset of adverse nonlinear effects [47]. This constraint introduces an immediate benefit in sensitivity via an increased total laser power budget, and, additionally, the smaller scale factor for each Sagnac interferometer increases the FOG dynamic range [33]. We investigate the additional enhancement in sensitivity that is possible when squeezed light is injected into a distributed FOG. While CV entanglement does not provide a significant sensitivity advantage over an optimized classical system when the total fiber length is unconstrained, we find that it can yield an appreciable improvement under a total fiber length constraint.

A. Distributed FOG modalities

In Fig. 4 we show three distributed FOG configurations. In all three cases, the M interferometers are fed by modes $\hat{a}_{\mathrm{in},j}$, $j \in [1, M]$, in coherent states $|\psi_{a,j}\rangle = |\alpha/\sqrt{M}\rangle$. These coherent states could be sourced from a single laser driving the coherent state $|\psi_{a'}\rangle = |\alpha\rangle$ in mode $\hat{a}'_{\mathrm{in},1}$ with mean photon number $N_v \equiv \langle\psi_a|\hat{a}'^{\dagger}_{\mathrm{in},1}\hat{a}'_{\mathrm{in},1}|\psi_{a'}\rangle = \alpha^2$, where this laser light is equally split M ways using a balanced beam splitter array (B in Fig. 4). An identical beam splitter array recombines the M symmetric output modes $\hat{b}_{\mathrm{out},j}$, and a single homodyne measurement is performed on mode $\hat{b}'_{\mathrm{out},1}$ [32]. The statistics of the output variable $\tilde{b}'_{\mathrm{out},1}$ from a quantum-noise-limited, lossless, imaginary-quadrature homodyne measurement are calculated in Appendix B for each of the three configurations.

A distributed classical FOG (design D) is depicted in Fig. 4(a). The $\hat{b}_{\mathrm{in},j}$ mode on each interferometer is in a vacuum state $|\psi_b\rangle = |0\rangle$, and the joint quantum state is $|\psi_{a'}\rangle|\psi_b\rangle^{\otimes M}$, with $\otimes M$ denoting a tensor product. Since coherent states and vacuum states remain pure through passive linear optical transformations such as the beam splitter arrays B, the light effectively undergoes the same evolution as that of design C, with homodyne output statistics given by Eq. (4). If η is the optical transmissivity of each identical interferometer, the variance of the unbiased estimator $\tilde{\Omega}_{\mathrm{D}} = 2\tilde{b}'_{\mathrm{out},1}/(T\sqrt{\eta}\alpha)$ is given by

$$\langle\Delta\tilde{\Omega}^2_{\mathrm{D}}\rangle \approx \frac{1}{T^2\eta\alpha^2} = \frac{1}{V^{-2}n_v}\frac{M}{L^2 10^{-bL/10M}}. \tag{16}$$

In the simplest squeezing-enhanced, distributed FOG (design P), identical SV states $|\psi_b\rangle = |0; -r\rangle$ are introduced independently into each of the M interferometers [Fig. 4(b)]. The optical input to this system is again in the product state $|\psi_{a'}\rangle|\psi_b\rangle^{\otimes M}$, where the total mean photon number from the squeezed light is $N_s = \sum_{j=1}^{M}\langle\psi_b|\hat{b}^{\dagger}_{\mathrm{in},j}\hat{b}_{\mathrm{in},j}|\psi_b\rangle = M\sinh^2(r)$. The mean and variance of the homodyne output variable $\tilde{b}'^2_{\mathrm{out},1}$ take the same form as that of design S [Eq. (7)], with the variance depending on the squeezing parameter r of just one of the M SV states $|\psi_b\rangle$ (Appendix B). Using the unbiased estimator $\tilde{\Omega}_{\mathrm{P}} = 2\tilde{b}'_{\mathrm{out},1}/(T\sqrt{\eta}\alpha)$,

$$\langle\Delta\tilde{\Omega}^2_{\mathrm{P}}\rangle \approx \frac{1}{V^{-2}n_v}\frac{M}{L^2 10^{-bL/10M}} \times\left(\frac{10^{-bL/10M}}{(\sqrt{1+N_s/M}+\sqrt{N_s/M})^2}+1-10^{-bL/10M}\right). \tag{17}$$

Finally, in Fig. 4(c) we show the design of our proposed CV entanglement-enhanced FOG (design E). Entangled light is generated by symmetrically splitting a single-mode SV state with mean photon-unit energy equal to $N_s = \langle\psi_b|\hat{b}'^{\dagger}_{\mathrm{in},1}\hat{b}'_{\mathrm{in},1}|\psi_{b'}\rangle = \sinh^2(r)$ using another balanced beam splitter array B [20], the output of which is distributed to the M interferometers. The resulting $\hat{b}_{\mathrm{in},j}$ modes exhibit mutual quantum entanglement and cannot be written as a tensor product of quantum states. In Appendix B we show that $\hat{a}'_{\mathrm{in},1}$ and $\hat{b}'_{\mathrm{in},1}$ evolve into $\hat{a}'_{\mathrm{out},1}$ and $\hat{b}'_{\mathrm{out},1}$ via the exact

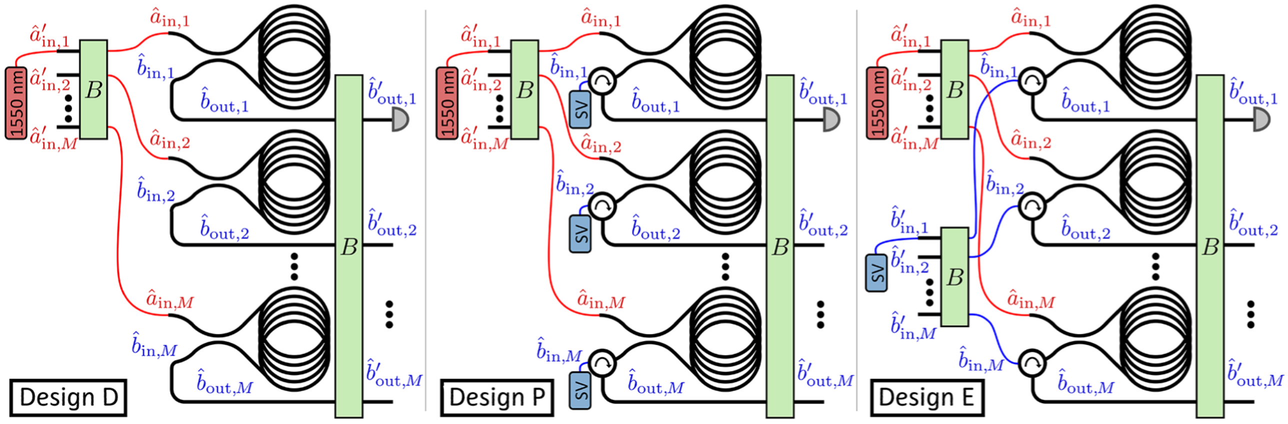

FIG. 4. (a) Distributed classical FOG (design D) with each interferometer fed by the same laser. (b) Product-state squeezing-enhanced FOG (design P) with separable SV inputs generated using M single-mode squeezers. (c) Entanglement-enhanced FOG (design E) with a SV from one squeezer distributed to the M interferometers. While the Sagnac loops are drawn as separated in space, in practice they could be mounted on the same fiber spool with independent fiber couplers.

same mathematical relationships as for design S, so the mean and variance of the homodyne measurement output $\tilde{b}'_{\text{out},1}$ are given by expressions equivalent to Eqs. (2) and (3). The unbiased estimator $\langle \Delta\tilde{\Omega}^2_{\text{E}}\rangle = 2\tilde{b}'_{\text{out},1}/(T\sqrt{\eta}\alpha)$ has a variance of

$$\langle \Delta\tilde{\Omega}^2_{\text{E}}\rangle \approx \frac{1}{V^{-2}n_v}\frac{M}{L^2 10^{-bL/10M}} \times \left(\frac{10^{-bL/10M}}{(\sqrt{1+N_s}+\sqrt{N_s})^2} + 1 - 10^{-bL/10M}\right). \tag{18}$$

Comparing Eqs. (17) and (18), the sensitivity achieved by design E depends on the entire squeezed energy budget N_s, whereas the effective contribution to the sensitivity of design P is only $1/M$ of the total squeezed light.

B. Quantum-enhanced distributed FOG sensitivity with unconstrained total fiber length

For design D with $\eta = 10^{-bL/10}$, minimizing the estimator variance [Eq. (16)] over the total fiber length by solving $\partial\langle \Delta\tilde{\Omega}^2_{\text{D}}\rangle/\partial L = 0$ gives the optimal total length

$$L_{\text{opt}} = \frac{20M}{\ln(10)b} \approx \frac{8.686M}{b}, \tag{19}$$

which equals the optimal total length for design C [Eq. (11)] scaled by M. The minimized variance is then

$$\langle \Delta\tilde{\Omega}^2_{\text{D}}\rangle|_{L=L_{\text{opt}}} = \frac{1}{V^{-2}Mn_v}\frac{e^2\ln(10)^2b^2}{400}, \tag{20}$$

a factor of M reduced from $\langle \Delta\tilde{\Omega}^2_{\text{C}}\rangle|_{L=L_{\text{opt}}}$ [Eq. (12)], since n_v is equal to N_v when using a single interferometer.

Optimizing the total fiber length for design E reveals a similar relationship with respect to design S. Solving $\partial\langle \Delta\tilde{\Omega}^2_{\text{E}}\rangle/\partial L = 0$ using Eq. (18) gives

$$L_{\text{opt}} = \frac{10[2+\Lambda(N_s)]M}{\ln(10)b}, \tag{21}$$

the optimal fiber length for design S [Eq. (13)] scaled by M. This is evidence that design E is the true distributed sensing analog for a squeezing-enhanced FOG. Likewise,

$$\langle \Delta\tilde{\Omega}^2_{\text{E}}\rangle|_{L=L_{\text{opt}}} = \frac{1}{V^{-2}Mn_v}\frac{e^{2+\Lambda(N_s)}\ln(10)^2b^2}{200[2+\Lambda(N_s)]}, \tag{22}$$

equivalent to $(1/M)\langle \Delta\tilde{\Omega}^2_{\text{S}}\rangle|_{L=L_{\text{opt}}}$ [Eq. (15)].

For design P, the equation $\partial\langle \Delta\tilde{\Omega}^2_{\text{P}}\rangle/\partial L = 0$ can be solved using Eq. (17) to obtain

$$L_{\text{opt}} = \frac{10[2+\Lambda(N_s/M)]M}{\ln(10)b}. \tag{23}$$

The optimized estimator variance is

$$\langle \Delta\tilde{\Omega}^2_{\text{P}}\rangle|_{L=L_{\text{opt}}} = \frac{1}{V^{-2}Mn_v}\frac{e^{2+\Lambda(N_s/M)}\ln(10)^2b^2}{200[2+\Lambda(N_s/M)]}, \tag{24}$$

which has no simple relationship with $\langle \Delta\tilde{\Omega}^2_{\text{S}}\rangle|_{L=L_{\text{opt}}}$.

In Fig. 5 we compare the sensitivity of these three distributed FOG modalities when the total available fiber length L is optimized for each case. Since the input laser power scales with M, distributed sensing yields an immediate advantage independent of squeezing, as seen for design D (black bars). Given a fixed total energy budget from squeezed light N_s, design E (cyan bars) increasingly outperforms design P (red bars) as M increases. Alternatively, the *per-mode* energy n_s of each injected SV state could be held fixed; this is the case if all available single-mode squeezing sources generate SV states at σ dB of squeezing, for example. In this case, design P (magenta bars), for which $n_s = N_s/M$, matches the sensitivity of design E, for which $n_s = N_s$, for all values of M. However, to match this performance, design P requires M physical single-mode squeezers, each producing the same amount of squeezing as that of the one squeezer used for design E (Fig. 4). This result showcases the value of entanglement-enhanced sensing in terms of resource efficiency: using

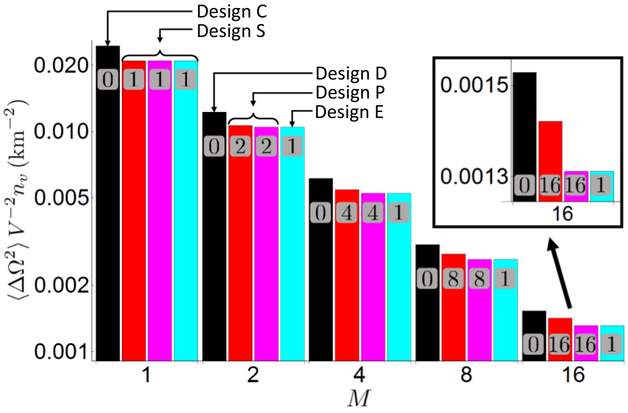

FIG. 5. Normalized rotation estimator variance of distributed FOG modalities with optimized total fiber length and $b = 0.5$ dB/km of loss. Black bars indicate design D. Red bars indicate design P with total squeezed-light energy equivalent to the energy from a single 10 dB squeezer. Magenta bars indicate design P with M 10 dB squeezers. Cyan bars indicate design E using a single 10 dB squeezer. Numbers within bars indicate the number of single-mode squeezers required to implement the FOG design. Inset: Magnified view of results for $M = 16$.

CV quantum entanglement, a single SV source enables the same quantitative performance as that achieved by several of the same SV sources placed in parallel, which collectively generate M-fold more squeezed photons. Still, the additional improvements arising from an injected SV for designs P and E over design D are only marginal regardless of M.

C. Quantum-enhanced distributed FOG sensitivity with constrained total fiber length

Gyroscopes are often employed in navigation or inertial tracking contexts with strict requirements on the total allowable payload and/or a maximum size restriction for the device. For a FOG with a fixed diameter, these weight and size constraints will dictate a maximum total fiber length L allowed for the gyroscope, assuming that fiber couplers, beam splitters, and integrated optical sources and detectors account for a relatively small footprint. For each of the three distributed FOG modalities depicted in Fig. 4, the design parameter M can be tuned to optimally balance the input coherent state amplitude $\alpha = \sqrt{Mn_v}$, the fiber transmissivity $\eta = 10^{-bL/10M}$, and the number of area-contributing fiber loops for each interferometer $m = L/(2\pi rM)$.

Using Eq. (16) for design D and solving $\partial\langle\Delta\tilde{\Omega}_{\mathrm{D}}^2\rangle/\partial M = 0$, the optimal number of distributed interferometers depends on the fiber length constraint L and is given by

$$M_{\mathrm{opt}} = \frac{bL\ln(10)}{10} \approx 0.23bL. \tag{25}$$

Consequently, the optimized estimator variance is

$$\langle\Delta\tilde{\Omega}_{\mathrm{D}}^2\rangle|_{M=M_{\mathrm{opt}}} = \frac{be\ln(10)}{10L}. \tag{26}$$

For design E, the equation $\partial\langle\Delta\tilde{\Omega}_{\mathrm{E}}^2\rangle/\partial M = 0$ can be solved using Eq. (18) to obtain

$$M_{\mathrm{opt}} = \frac{bL\ln(10)}{10[1+\Gamma(N_s)]} \tag{27}$$

and

$$\langle\Delta\tilde{\Omega}_{\mathrm{E}}^2\rangle|_{M=M_{\mathrm{opt}}} = \frac{be^{1+\Gamma(N_s)}\ln(10)}{10L}, \tag{28}$$

where

$$\Gamma(x) = W\left(\frac{2[x-\sqrt{x(1+x)}]}{e}\right). \tag{29}$$

A similar optimization for design P can be performed numerically. Since $\langle\Delta\tilde{\Omega}_{\mathrm{D}}^2\rangle$, $\langle\Delta\tilde{\Omega}_{\mathrm{P}}^2\rangle$, and $\langle\Delta\tilde{\Omega}_{\mathrm{E}}^2\rangle$ are convex, the optimal multiplexing configuration for each design can be obtained by rounding M_{opt} either down or up to the nearest positive integer, whichever yields the lower estimator variance. If this procedure yields $M_{\mathrm{opt}} = 1$, distributed sensing offers no benefit; design D becomes design C, and designs P and E both equate to design S.

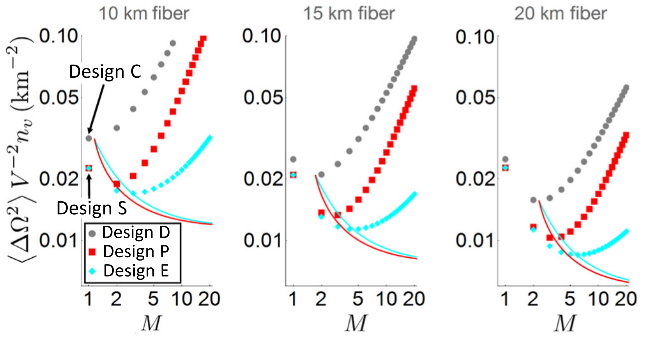

FIG. 6. Normalized rotation estimate variance as a function of M for design D (gray), design P FOG (red), and design E (cyan) with given total fiber length constraints. In each case, $b = 0.5$ dB loss/km of fiber. The design E results use 10 dB of squeezing. For the design P results, the mean photon number N_s from all injected SVs is equal to that of a single-mode SV with 10 dB squeezing. The descending solid parametric curves give rotation estimate variances with optimized M as the squeezing is increased.

The effect of this trade-off on rotation sensitivity is visualized in Fig. 6 for three fixed total fiber lengths and 10 dB of squeezing. As the available fiber length is increased, the sensitivity achieved by all three distributed FOG designs improves, as expected. We find that adding one or two sensors will only improve design D over design C in the case of very long total fiber lengths, whereas designs P and E obtain a greater benefit in sensitivity from multiplexing several interferometers. Design E reaches the best rotation sensitivity, with an optimal number of interferometers M_{opt} that increases both with the total fiber length and with the amount of squeezing, but remains a reasonable $M_{\mathrm{opt}} \approx 5$ for 10 dB of squeezing. The resulting decrease in the fiber length of each Sagnac interferometer also increases the unambiguous dynamic range of the FOG [33]. The sensitivity of design P is worse than that of design E when the total squeezed energy N_s is held fixed. As seen in Fig. 5, design P again matches the performance of design E if the per-mode squeezed energy n_s is consistent between the two designs, but it does so at the cost of using M single-mode squeezers and additional pump energy.

V. COMPARISON OF QUANTUM-ENHANCED AND CLASSICAL FOG SENSITIVITY

While none of the FOG modalities described here exhibit a Heisenberg scaling advantage in the presence of fiber loss, in this section we identify circumstances under which quantum enhancement can still enable notable constant-factor improvements over the SQL. We define rotation estimator variance ratios $R_{\mathrm{S}} = \langle\Delta\tilde{\Omega}^2_{\mathrm{S}}\rangle/\langle\Delta\tilde{\Omega}^2_{\mathrm{C}}\rangle$, $R_{\mathrm{P}} = \langle\Delta\tilde{\Omega}^2_{\mathrm{P}}\rangle/\langle\Delta\tilde{\Omega}^2_{\mathrm{D}}\rangle$, and $R_{\mathrm{E}} = \langle\Delta\tilde{\Omega}^2_{\mathrm{E}}\rangle/\langle\Delta\tilde{\Omega}^2_{\mathrm{D}}\rangle$ of designs S, P, and E against the corresponding classical FOGs using Eqs. (6), (10), (16), (17), and (18). We stress that the baseline comparison for designs P and E is design D, so the M-fold reduction in estimator variance gained from increased laser power is canceled out in R_{P} and R_{E}. As a result, the estimator variance ratios isolate the advantage arising from quantum enhancement.

A. Sensitivity comparison for 15 km fiber

As an example, in Fig. 7 we plot the three estimator variance ratios R_{S}, R_{P}, and R_{E} for a realistic total fiber length requirement of $L = 15$ km. While squeezing with a single interferometer (design S) provides some improvement over the single-mode SQL (design C), adding multiple distributed sensors augments the benefits of quantum enhancement. Comparing the quantum-enhanced FOG designs, the greatest performance gap between our design E and the design P occurs with five or more multiplexed interferometers and 5–15 dB of single-mode squeezing, which are reasonable design parameters for a next-generation quantum sensing system. Moreover, while the high-squeezing behavior $\lim_{N_s\to\infty}\{R_{\mathrm{S}}\} = \lim_{N_s\to\infty}\{R_{\mathrm{P}}\} = \lim_{N_s\to\infty}\{R_{\mathrm{E}}\} = 1-\eta$ is recovered, design E converges to this performance with a much lower energy requirement for squeezed light compared with design P.

B. Estimator variance ratios for optimized CV entanglement-enhanced FOGs

Lastly, we focus on the performance of our CV entanglement-enhanced FOG design compared with the SQL. We analytically calculate the estimator variance ratios for optimized sensor configurations under two scenarios: when the total fiber length is not constrained and when it is constrained to a fixed length. Additionally, we consider here the system loss accumulated in a real FOG from fiber coupling and homodyne detection and model the aggregate transmissivity from these sources using κ. For the derivations in the main text, we assume that $\kappa = 1$, while analytical results for $\kappa < 1$ are derived in Appendix C.

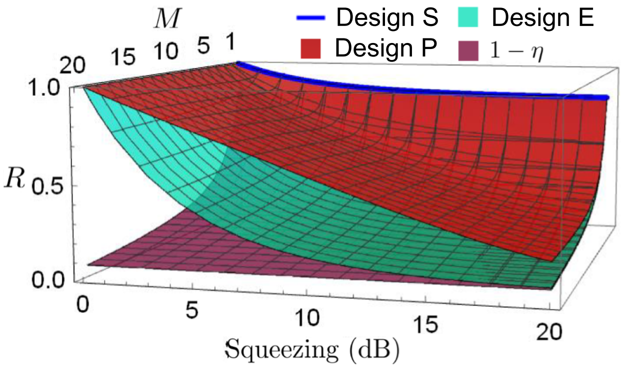

FIG. 7. Estimator variance ratios R_{S} (blue parametric curve), R_{P} (red surface), and R_{E} (cyan surface) as a function of squeezing and the number of interferometers for $b = 0.5$ dB loss/km fiber and a total fiber length constraint $L = 15$ km. For the R_{P} results, the mean photon number N_s from all injected squeezed states is equal to that of a single-mode SV state with squeezing given by the x axis. The purple surface shows $1-\eta = 1-10^{-b(L/M)/10}$ for reference.

If the total fiber length is unconstrained and can be optimized, $R_{\mathrm{E}}|_{L=L_{\mathrm{opt}}} = \langle\Delta\tilde{\Omega}^2_{\mathrm{E}}\rangle|_{L=L_{\mathrm{opt}}}/\langle\Delta\tilde{\Omega}^2_{\mathrm{D}}\rangle|_{L=L_{\mathrm{opt}}}$ gives the ratio between the estimator variance of design E [Eq. (22)] and that of design D [Eq. (20)], where each estimator variance is calculated with optimized fiber length. Interestingly, this ratio is found to be

$$R_{\mathrm{E}}|_{L=L_{\mathrm{opt}}} = \frac{2e^{\Lambda(N_s)}}{2+\Lambda(N_s)}, \tag{30}$$

which depends on neither n_v, b, nor M, but is determined solely by the squeezing in the injected SV. In particular, since $R_{\mathrm{E}}|_{L=L_{\mathrm{opt}}}$ is the same for all M including $M = 1$, it is equivalent to the variance ratio $R_{\mathrm{S}}|_{L=L_{\mathrm{opt}}}$ of a single-mode squeezing-enhanced FOG (design S) compared with the single-mode SQL (design C). In the high-squeezing limit, the variance ratio converges to

$$\lim_{N_s\to\infty}\{R_{\mathrm{E}}|_{L=L_{\mathrm{opt}}}\} = \frac{2e^{W(-2/e^2)}}{2+W(-2/e^2)} \approx 0.836, \tag{31}$$

which lower bounds the constant-factor drop in estimator variance below the SQL with unconstrained fiber length.

When the total fiber length L is constrained to a fixed value, $R_{\mathrm{E}}|_{M=M_{\mathrm{opt}}} = \langle\Delta\tilde{\Omega}^2_{\mathrm{E}}\rangle|_{M=M_{\mathrm{opt}}}/\langle\Delta\tilde{\Omega}^2_{\mathrm{D}}\rangle|_{M=M_{\mathrm{opt}}}$ gives the ratio between the estimator variances of designs E [Eq. (28)] and D [Eq. (26)]. The resulting ratio

$$R_{\mathrm{E}}|_{M=M_{\mathrm{opt}}} = e^{\Gamma(N_s)} \tag{32}$$

depends only on N_s, not on n_v, b, nor L. Since the variances are optimized with $M_{\mathrm{opt}} \geq 1$, in general, this advantage is not achieved by design S and requires the use of distributed sensing. Remarkably, the high-squeezing limit gives the simple lower bound

$$\lim_{N_s\to\infty}\{R_{\mathrm{E}}|_{M=M_{\mathrm{opt}}}\} = e^{-1} \approx 0.368, \tag{33}$$

the fundamental reduction in rotation estimator variance below the multimode SQL that is achievable with our entanglement-enhanced FOG design.

In Fig. 8 we plot the estimator variance ratios for our entanglement-enhanced design in these two cases, while in Table I we give the constant-factor improvement, i.e., the inverse of the variance ratio, that can be achieved with

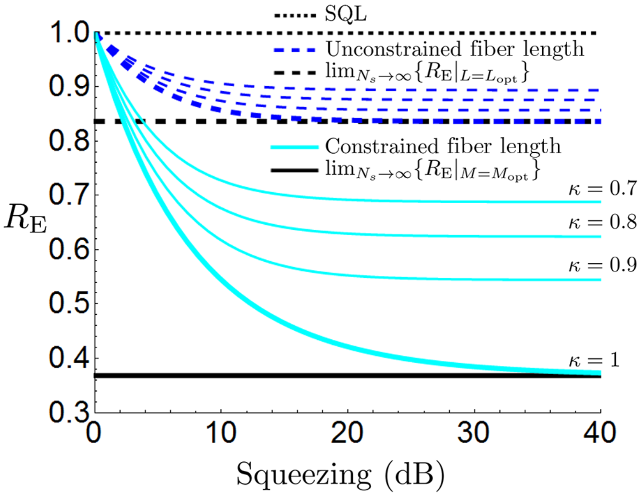

FIG. 8. The ratio R_E between angular-velocity estimator variances for entanglement-enhanced and classical FOGs as a function of single-mode squeezing. Results are independent of b. Design E with unconstrained fiber length achieves a best sensitivity ratio of 0.836 compared with the SQL (design D). Design E achieves a minimum ratio of $e^{-1} \approx 0.368$ under a fixed total fiber length constraint. System loss (thinner lines from bottom to top indicate $\kappa = 0.9$, $\kappa = 0.8$, $\kappa = 0.7$) results in tempered quantum advantage.

respect to the SQL. With unconstrained fiber length, which is when the variance ratio for design E conforms to that for design S, a currently realizable 10–15 dB of squeezing attains a constant-factor improvement nearly equal to the fundamental maximum factor of 1.196. However, this best-case constant-factor improvement is practically negligible, so the system demonstrated in Ref. [39] has limited useful potential for reducing the rotation estimate variance below the SQL.

On the other hand, under the realistic constraint of fixed fiber length with an optimized number of interferometers, an appreciable advantage over classical sensing is possible, as the constant-factor improvement for our design E over design D in this case is upper bounded by $e = 2.718$. CV entanglement is required to access this gain in performance (Fig. 6), which holds regardless of the total fiber length requirement or the characteristic fiber loss but is degraded somewhat by realistic system losses. The maximum improvement for a given amount of system loss κ is achieved only at infinite squeezing, but most of this gain is attainable at 10–15 dB of squeezing (Fig. 8). As a result, our CV entanglement-enhanced FOG design could reach meaningfully sub-SQL rotation precision with currently existing squeezing technology.

TABLE I. Constant-factor improvement in rotation sensitivity (given $\kappa = 1$) for the entanglement-enhanced FOG over the SQL under a total fiber length optimization (first row) or a total fiber length constraint with an optimized number of interferometers (second row).

	Squeezing (dB)				
	5	10	15	20	∞
$R_E\|_{L=L_{opt}}^{-1} = R_S\|_{L=L_{opt}}^{-1}$	1.116	1.168	1.187	1.193	1.196
$R_E\|_{M=M_{opt}}^{-1}$	1.435	1.837	2.154	2.375	2.718

VI. DISCUSSION

Our work expands upon the use of quadrature squeezing to show that CV entanglement further improves peak performance in a high-precision sensing application under realistic conditions. Our proposed design E is an application of recent theoretical works on CV entanglement-enhanced sensitivity for interferometric sensors [20,23–27], which emphasize the achievability of Heisenberg scaling in sensitivity. Our results show that entanglement can provide the additional benefit of matching the quantum advantage of nonentangled quantum sensors with a lower quantum resource (i.e., squeezing) requirement. While the optimal per-photon performance for such systems is achieved with just a SV input [23], Heisenberg scaling in sensitivity is also known to be possible using the SV and coherent state probes considered here, a configuration which also enables high laser power [20,27]. Notably, the quantitative enhancement from entanglement depends on the parametric model of the specific physical system [27,30]. For example, the improvement factors over classical FOGs that we report here result from the characteristic balance between scale factor and fiber loss for fiber Sagnac interferometers; CV entanglement may benefit other sensing applications even more.

While none of the sensor designs evaluated here achieve Heisenberg-limited scaling in sensing performance due to fiber loss, we have shown that FOG rotation sensitivity can be boosted beyond the SQL by useful constant factors using CV quantum entanglement that are not possible with a single squeezing-enhanced Sagnac interferometer. Our analysis considers currently feasible specifications on single-mode squeezing, optical gyroscope, and homodyne detection technologies; in fact, our results indicate that additional improvements in single-mode squeezing capabilities would yield diminishing returns in rotation sensitivity. We conclude that an entanglement-enhanced FOG is a promising near-term technology that could both demonstrate the benefits of quantum sensing and potentially provide useful improvements to high-sensitivity inertial tracking systems under practical, real-world constraints, such as size or payload limitations.

A key advantage of our CV entanglement-enhanced FOG design is access to quantum-enhanced distributed sensing with only one single-mode squeezer. While a squeezing device could add to the total weight of a FOG setup, the ability to generate squeezed vacuum states would reduce the footprint compared with the optical fiber, although potentially at the cost of increased fiber coupling loss. An additional possibility could be generation of squeezed light inside of a cavity or within the optical fiber itself to reduce coupling losses. Finally, nonreciprocal phase accumulation due to scattering [48], polarization nonreciprocity, and nonlinear Kerr effects [33] can be a significant source of error for FOG technologies and should be taken into account in future work.

The role of distributed sensing could be impactful for future technologies including FOGs. Indeed, entanglement could improve the performance of a FOG in inertial sensing contexts, such as terrestrial, naval, aircraft, and space-based navigation. Additionally, for coordinated movements with distant FOG systems, preshared entanglement could be used to register individual gyroscopes to each other. An experimental demonstration of our scheme is within reach and would make progress toward yet another increase of real-world technological capability using quantum-enhanced sensing.

ACKNOWLEDGMENTS

This work was supported by the Office of Naval Research (ONR) under a 6.2 Quantum Information Science (QIS) project funded to University of Arizona, under Contract No. N00014-19-1-2189. The authors acknowledge valuable discussions with Zheshen Zhang, Linran Fan, and Khanh Kieu.

APPENDIX A: CONJUGATE PHASE SENSING THEORY

Here, we derive the output statistics of a quantum-noise-limited, lossless homodyne measurement when the two arms of a conjugate phase sensing MZI are symmetrically affected by pure optical loss with transmissivity η on each arm. In a conjugate phase sensing setup, such as a FOG of design C or S, the optical field operators $\hat{a}_{\mathrm{in}}$ and $\hat{b}_{\mathrm{in}}$ evolve through the system via unitary dynamics in the Heisenberg picture. The unitary transformation applied by the quantum circuit in the inset of Fig. 1 is

$$\begin{aligned} U(\phi) &= \frac{1}{\sqrt{2}}\begin{bmatrix} 1 & 1 \\ -1 & 1 \end{bmatrix}\begin{bmatrix} e^{-i\phi} & 0 \\ 0 & e^{i\phi} \end{bmatrix}\frac{1}{\sqrt{2}}\begin{bmatrix} 1 & 1 \\ 1 & -1 \end{bmatrix} \\ &= \begin{bmatrix} \cos(\phi) & -i\sin(\phi) \\ i\sin(\phi) & -\cos(\phi) \end{bmatrix}, \end{aligned} \tag{A1}$$

where $i = \sqrt{-1}$. Equation (A1) holds for both discrete-variable and CV quantum states.

Assuming symmetric loss processes that impose equal transmissivities η on the two opposing paths around the fiber coil, we model fiber loss with the pure-loss channel

$$\Phi_\eta\left(\begin{bmatrix} \hat{a}_{\mathrm{in}} \\ \hat{b}_{\mathrm{in}} \end{bmatrix}\right) = \begin{bmatrix} \sqrt{\eta}\hat{a}_{\mathrm{in}} + \sqrt{1-\eta}\hat{e}_a \\ \sqrt{\eta}\hat{b}_{\mathrm{in}} + \sqrt{1-\eta}\hat{e}_b \end{bmatrix}, \tag{A2}$$

where $\hat{e}_k$ signifies an ancillary vacuum mode that is associated with the optical mode $\hat{k}_{\mathrm{in}}$. For any Gaussian state, a pure-loss channel with equal loss for each mode commutes with any passive unitary operation, so the loss channel Φ_η can be applied directly on the input modes $\hat{a}_{\mathrm{in}}$ and $\hat{b}_{\mathrm{in}}$. The output field operators for a FOG become

$$\begin{aligned} \begin{bmatrix} \hat{a}_{\mathrm{out}} \\ \hat{b}_{\mathrm{out}} \end{bmatrix} &= U(\phi)\Phi_\eta\left(\begin{bmatrix} \hat{a}_{\mathrm{in}} \\ \hat{b}_{\mathrm{in}} \end{bmatrix}\right) \\ &= \begin{bmatrix} \begin{array}{l} \cos(\phi)[\sqrt{\eta}\hat{a}_{\mathrm{in}} + \sqrt{1-\eta}\hat{e}_a] \\ \quad -i\sin(\phi)[\sqrt{\eta}\hat{b}_{\mathrm{in}} + \sqrt{1-\eta}\hat{e}_b] \\ i\sin(\phi)[\sqrt{\eta}\hat{a}_{\mathrm{in}} + \sqrt{1-\eta}\hat{e}_a] \\ \quad -\cos(\phi)[\sqrt{\eta}\hat{b}_{\mathrm{in}} + \sqrt{1-\eta}\hat{e}_b] \end{array} \end{bmatrix}. \end{aligned} \tag{A3}$$

A homodyne measurement on the imaginary quadrature of mode $\hat{b}_{\mathrm{out}}$ is sufficient to estimate ϕ for given input states $|\psi_a\rangle$ and $|\psi_b\rangle$. If the homodyne measurement is quantum-noise limited, the classical random variable $\tilde{b}_{\mathrm{out}}$ will inherit the statistics of $\mathrm{Im}(\hat{b}_{\mathrm{out}})$. Its mean is

$$\begin{aligned} \langle\tilde{b}_{\mathrm{out}}\rangle &= \langle\mathrm{Im}(\hat{b}_{\mathrm{out}})\rangle \\ &= \sin(\phi)[\sqrt{\eta}\langle\mathrm{Re}(\hat{a}_{\mathrm{in}})\rangle + \sqrt{1-\eta}\langle\mathrm{Re}(\hat{e}_a)\rangle] \\ &\quad - \cos(\phi)[\sqrt{\eta}\langle\mathrm{Im}(\hat{b}_{\mathrm{in}})\rangle + \sqrt{1-\eta}\langle\mathrm{Im}(\hat{e}_b)\rangle] \\ &= \sqrt{\eta}[\sin(\phi)\langle\mathrm{Re}(\hat{a}_{\mathrm{in}})\rangle - \cos(\phi)\langle\mathrm{Im}(\hat{b}_{\mathrm{in}})\rangle] \end{aligned} \tag{A4}$$

and its variance is

$$\begin{aligned} \langle\Delta\tilde{b}_{\mathrm{out}}^2\rangle &= \langle\mathrm{Im}(\hat{b}_{\mathrm{out}})^2\rangle - \langle\mathrm{Im}(\hat{b}_{\mathrm{out}})^2\rangle \\ &= \sin(\phi)^2[\eta\langle\mathrm{Re}(\hat{a}_{\mathrm{in}})^2\rangle + (1-\eta)\langle\mathrm{Re}(\hat{e}_a)^2\rangle] \\ &\quad + \cos(\phi)^2[\eta\langle\mathrm{Im}(\hat{b}_{\mathrm{in}})^2\rangle + (1-\eta)\langle\mathrm{Im}(\hat{e}_b)^2\rangle] \\ &\quad - \sin(\phi)^2[\eta\langle\mathrm{Re}(\hat{a}_{\mathrm{in}})\rangle^2 + (1-\eta)\langle\mathrm{Re}(\hat{e}_a)\rangle^2] \\ &\quad - \cos(\phi)^2[\eta\langle\mathrm{Im}(\hat{b}_{\mathrm{in}})\rangle^2 + (1-\eta)\langle\mathrm{Im}(\hat{e}_b)\rangle^2] \\ &= \eta[\sin(\phi)^2\langle\Delta\mathrm{Re}(\hat{a}_{\mathrm{in}})^2\rangle + \cos(\phi)^2\langle\Delta\mathrm{Im}(\hat{b}_{\mathrm{in}})^2\rangle] \\ &\quad + \frac{1-\eta}{4}. \end{aligned} \tag{A5}$$

Quantum vacuum state quadratures exhibit a zero mean field $[\langle\mathrm{Re}(\hat{e}_a)\rangle = \langle\mathrm{Im}(\hat{e}_b)\rangle = 0]$ but nonzero variance $[\langle\Delta\mathrm{Re}(\hat{e}_a)^2\rangle = \langle\Delta\mathrm{Im}(\hat{e}_b)^2\rangle = 1/4]$, the latter being a direct consequence of the quantum uncertainty principle.

APPENDIX B: DISTRIBUTED CONJUGATE PHASE SENSING

Since the output modes $\hat{b}_{\mathrm{out},j}$ of each MZI are all identical due to the symmetry across all M modes, a balanced beam splitter array will fully recombine all of the light into mode $\hat{b}'_{\mathrm{out},1}$. Additional optimization of the recombination step [25,26] would not provide any benefit for any of our three distributed FOG designs. A distributed FOG with separable inputs to each interferometer (e.g., designs D and P) can be thought of as a series of conjugate phase sensors. After recombination, we have

$$\begin{aligned}\hat{b}'_{\mathrm{out},1} &= i\sin(\phi)(\sqrt{\eta}\hat{a}'_{\mathrm{in},1} + \sqrt{1-\eta}\hat{e}'_{a,1})\\ &\quad - \frac{\cos(\phi)}{\sqrt{M}}\sum_{j}^{M}(\sqrt{\eta}\hat{b}_{\mathrm{in},j} + \sqrt{1-\eta}\hat{e}_{b,j}). \end{aligned} \tag{B1}$$

A quantum-noise-limited homodyne measurement on the imaginary quadrature of mode $\hat{b}'_{\mathrm{out},1}$ then has mean

$$\begin{aligned}\langle\tilde{b}'_{\mathrm{out},1}\rangle &= \langle\mathrm{Im}(\hat{b}'_{\mathrm{out},1})\rangle\\ &= \sin(\phi)\left[\sqrt{\eta}\langle\mathrm{Re}(\hat{a}'_{\mathrm{in}_1})\rangle + \sqrt{1-\eta}\langle\mathrm{Re}(\hat{e}'_{a,1})\rangle\right]\\ &\quad - \frac{\cos(\phi)}{\sqrt{M}}\sum_{j}^{M}\left[\sqrt{\eta}\langle\mathrm{Im}(\hat{b}_{\mathrm{in},j})\rangle + \sqrt{1-\eta}\langle\mathrm{Im}(\hat{e}_{b,j})\rangle\right]\\ &= \sqrt{\eta}\left[\sin(\phi)\langle\mathrm{Re}(\hat{a}'_{\mathrm{in}_1})\rangle - \frac{\cos(\phi)}{\sqrt{M}}\sum_{j}^{M}\langle\mathrm{Im}(\hat{b}_{\mathrm{in},j})\rangle\right] \end{aligned} \tag{B2}$$

and variance

$$\begin{aligned}\langle\Delta\tilde{b}'^{2}_{\mathrm{out},1}\rangle &= \langle\mathrm{Im}(\hat{b}'_{\mathrm{out},1})^2\rangle - \langle\mathrm{Im}(\hat{b}'_{\mathrm{out},1})\rangle^2\\ &= \sin(\phi)^2[\eta\langle\mathrm{Re}(\hat{a}'_{\mathrm{in},1})^2\rangle + (1-\eta)\langle\mathrm{Re}(\hat{e}_{a,1})^2\rangle]\\ &\quad + \frac{\cos(\phi)^2}{M}\sum_{j}^{M}[\eta\langle\mathrm{Im}(\hat{b}_{\mathrm{in},j})^2\rangle + (1-\eta)\langle\mathrm{Im}(\hat{e}_{b,j})^2\rangle]\\ &\quad - \sin(\phi)^2[\eta\langle\mathrm{Re}(\hat{a}'_{\mathrm{in},1})\rangle^2 + (1-\eta)\langle\mathrm{Re}(\hat{e}_{a,1})\rangle^2]\\ &\quad - \frac{\cos(\phi)^2}{M}\sum_{j}^{M}[\eta\langle\mathrm{Im}(\hat{b}_{\mathrm{in},j})\rangle^2 + (1-\eta)\langle\mathrm{Im}(\hat{e}_{b,j})\rangle^2]\\ &= \eta\left[\sin(\phi)^2\langle\Delta\mathrm{Re}(\hat{a}'_{\mathrm{in},1})^2\rangle + \frac{\cos(\phi)^2}{M}\sum_{j}^{M}\langle\Delta\mathrm{Im}(\hat{b}_{\mathrm{in},j})^2\rangle\right] + \frac{1-\eta}{4}. \end{aligned} \tag{B3}$$

If the separable quantum states injected into each mode $\hat{b}_{\mathrm{in},j}$ are identical, the quadrature variance has a nearly identical form to that from a single-mode interferometer [Eq. (A5)], except the first variance contribution comes from the state $|\psi_{a'}\rangle$ and the second is the variance of one copy of the state $|\psi_b\rangle$.

The injected SV in design E cannot be written as a series of separable quantum states. The input-output field operator relationship in this case is given by

$$\begin{aligned}\hat{b}'_{\mathrm{out},1} &= i\sin(\phi)(\sqrt{\eta}\hat{a}'_{\mathrm{in},1} + \sqrt{1-\eta}\hat{e}'_{a,1})\\ &\quad - \cos(\phi)(\sqrt{\eta}\hat{b}'_{\mathrm{in},1} + \sqrt{1-\eta}\hat{e}'_{b,1}), \end{aligned} \tag{B4}$$

which has the exact same form as the single-interferometer case [Eq. (A3)]. Since mode $\hat{b}'_{\mathrm{in},1}$ is the only SV state and has a mean photon number of N_s, the situation is identical to the development for design S (Sec. III A), and the same results for homodyne measurement statistics [Eqs. (A4) and (A5)] can be used, where $\tilde{b}_{\mathrm{out}}$ should be replaced with $\tilde{b}'_{\mathrm{out},1}$, $\hat{a}_{\mathrm{in}}$ with $\hat{a}'_{\mathrm{in},1}$, and $\hat{b}_{\mathrm{in}}$ with $\hat{b}'_{\mathrm{in},1}$.

APPENDIX C: ESTIMATOR VARIANCE RATIOS WITH SYSTEM LOSS

In addition to fiber loss, losses can occur in a laser-driven FOG from fiber coupling, homodyne detection, and other nonidealities. Assuming that these sources of system loss are identical across all optical modes in a FOG system, these losses can be mathematically commuted to act as an aggregate system loss κ along with the fiber loss η. The result is an overall pure-loss channel $\Phi_{\kappa\eta}$ that acts directly on the input modes of the FOG. Replacing η with $\kappa\eta$, the estimator variances for designs D [Eq. (16)] and E

[Eq. (18)] become

$$\begin{aligned}\langle\Delta\tilde{\Omega}_{\mathrm{D}}^2\rangle &\approx \frac{1}{V^{-2}n_v}\frac{M}{L^2\kappa 10^{-bL/10M}},\\ \langle\Delta\tilde{\Omega}_{\mathrm{E}}^2\rangle &\approx \frac{1}{V^{-2}n_v}\frac{M}{L^2\kappa 10^{-bL/10M}}\\ &\quad\times\left(\frac{\kappa 10^{-bL/10M}}{(\sqrt{1+N_s}+\sqrt{N_s})^2}+1-\kappa 10^{-bL/10M}\right).\end{aligned}\tag{C1}$$

When the total fiber length is not constrained, the rotation estimator variance can be optimized using the fiber lengths

$$\begin{aligned}L_{\mathrm{opt}} &= \frac{20M}{\ln(10)b} = \frac{8.686M}{b},\\ L_{\mathrm{opt}} &= \frac{10[2+\Lambda(N_s;\kappa)]M}{\ln(10)b}\end{aligned}\tag{C2}$$

for designs D and E, respectively, where

$$\Lambda(x;\kappa) = W\left(\frac{4\kappa[x-\sqrt{x(1+x)}]}{e^2}\right).\tag{C3}$$

The optimized fiber lengths yield estimator variances of

$$\begin{aligned}\langle\Delta\tilde{\Omega}_{\mathrm{D}}^2\rangle|_{L=L_{\mathrm{opt}}} &= \frac{1}{V^{-2}Mn_v}\frac{e^2\ln(10)^2b^2}{400\kappa},\\ \langle\Delta\tilde{\Omega}_{\mathrm{E}}^2\rangle|_{L=L_{\mathrm{opt}}} &= \frac{1}{V^{-2}Mn_v}\frac{e^{2+\Lambda(N_s;\kappa)}\ln(10)^2b^2}{200\kappa[2+\Lambda(N_s;\kappa)]},\end{aligned}\tag{C4}$$

resulting in the variance ratio

$$R_{\mathrm{E}}|_{L=L_{\mathrm{opt}}} = \frac{2e^{\Lambda(N_s;\kappa)}}{2+\Lambda(N_s;\kappa)},\tag{C5}$$

which depends only on N_s and κ and has the κ-dependent lower bound

$$\lim_{N_s\to\infty}\{R_{\mathrm{E}}|_{L=L_{\mathrm{opt}}}\} = \frac{2e^{W(-2\kappa/e^2)}}{2+W(-2\kappa/e^2)}.\tag{C6}$$

If the total fiber length is constrained to L km, the optimal numbers of interferometers for designs D and E are

$$\begin{aligned}M_{\mathrm{opt}} &= \frac{bL\ln(10)}{10} = 0.23bL,\\ M_{\mathrm{opt}} &= \frac{bL\ln(10)}{10[1+\Gamma(N_s;\kappa)]},\end{aligned}\tag{C7}$$

where

$$\Gamma(x;\kappa) = W\left(\frac{2\kappa[x-\sqrt{x(1+x)}]}{e}\right).\tag{C8}$$

The resulting optimized estimator variances are

$$\begin{aligned}\langle\Delta\tilde{\Omega}_{\mathrm{D}}^2\rangle|_{M=M_{\mathrm{opt}}} &= \frac{be\ln(10)}{10\kappa L},\\ \langle\Delta\tilde{\Omega}_{\mathrm{E}}^2\rangle|_{M=M_{\mathrm{opt}}} &= \frac{be^{1+\Gamma(N_s;\kappa)}\ln(10)}{10\kappa L},\end{aligned}\tag{C9}$$

and the estimator variance ratio

$$R_{\mathrm{E}}|_{M=M_{\mathrm{opt}}} = e^{\Gamma(N_s;\kappa)}\tag{C10}$$

depends only on N_s and κ with a lower bound of

$$\lim_{N_s\to\infty}\{R_{\mathrm{E}}|_{M=M_{\mathrm{opt}}}\} = e^{W(-\kappa/e)}.\tag{C11}$$

These estimator variance ratios are plotted in Fig. 8.

[1] S. Pirandola, B. R. Bardhan, T. Gehring, C. Weedbrook, and S. Lloyd, Advances in photonic quantum sensing, Nat. Photonics **12**, 724 (2018).

[2] V. Giovannetti, S. Lloyd, and L. MacCone, Advances in quantum metrology, Nat. Photonics **5**, 222 (2011).

[3] C. L. Degen, F. Reinhard, and P. Cappellaro, Quantum sensing, Rev. Mod. Phys. **89**, 035002 (2017).

[4] LIGO Scientific Collaboration, A gravitational wave observatory operating beyond the quantum shot-noise limit, Nat. Phys. **7**, 962 (2011).

[5] LIGO Scientific Collaboration and V. Collaboration, Observation of Gravitational Waves from a Binary Black Hole Merger, Phys. Rev. Lett. **116**, 061102 (2016).

[6] S. Lloyd, Enhanced sensitivity of photodetection via quantum illumination, Science **321**, 1463 (2008).

[7] S. H. Tan, B. I. Erkmen, V. Giovannetti, S. Guha, S. Lloyd, L. Maccone, S. Pirandola, and J. H. Shapiro, Quantum Illumination with Gaussian States, Phys. Rev. Lett. **101**, 253601 (2008).

[8] V. Giovannetti, S. Lloyd, and L. Maccone, Quantum-enhanced positioning and clock synchronization, Nature **412**, 417 (2001).

[9] S. Pirandola, Quantum Reading of a Classical Digital Memory, Phys. Rev. Lett. **106**, 090504 (2011).

[10] S. Guha and J. H. Shapiro, Reading boundless error-free bits using a single photon, Phys. Rev. A **87**, 062306 (2013).

[11] W. Wasilewski, K. Jensen, H. Krauter, J. J. Renema, M. V. Balabas, and E. S. Polzik, Quantum Noise Limited and Entanglement-Assisted Magnetometry, Phys. Rev. Lett. **104**, 133601 (2010).

[12] C. M. Caves, Quantum-mechanical noise in an interferometer, Phys. Rev. D **23**, 1693 (1981).

[13] R. S. Bondurant and J. H. Shapiro, Squeezed states in phase-sensing interferometers, Phys. Rev. D **30**, 2548 (1984).

[14] D. F. Walls, Squeezed states of light, Nature **306**, 141 (1983).

[15] H. P. Yuen and J. H. Shapiro, Generation and detection of two-photon coherent states in degenerate four-wave mixing, Opt. Lett. **4**, 334 (1979).

[16] C. Weedbrook, S. Pirandola, R. García-Patrón, N. J. Cerf, T. C. Ralph, J. H. Shapiro, and S. Lloyd, Gaussian quantum information, Rev. Mod. Phys. **84**, 621 (2012).

[17] G. Adesso, S. Ragy, and A. R. Lee, Continuous variable quantum information: Gaussian states and beyond, Open Syst. Inf. Dyn. **21**, 1440001 (2014).

[18] H. Vahlbruch, M. Mehmet, K. Danzmann, and R. Schnabel, Detection of 15 dB Squeezed States of Light and Their Application for the Absolute Calibration of Photoelectric Quantum Efficiency, Phys. Rev. Lett. **117**, 110801 (2016).

[19] A. Schönbeck, F. Thies, and R. Schnabel, 13 dB squeezed vacuum states at 1550 nm from 12 mW external pump power at 775 nm, Opt. Lett. **43**, 110 (2018).

[20] Q. Zhuang, Z. Zhang, and J. H. Shapiro, Distributed quantum sensing using continuous-variable multipartite entanglement, Phys. Rev. A **97**, 032329 (2018).

[21] W. Ge, K. Jacobs, Z. Eldredge, A. V. Gorshkov, and M. Foss-Feig, Distributed Quantum Metrology with Linear Networks and Separable Inputs, Phys. Rev. Lett. **121**, 043604 (2018).

[22] T. J. Proctor, P. A. Knott, and J. A. Dunningham, Multiparameter Estimation in Networked Quantum Sensors, Phys. Rev. Lett. **120**, 080501 (2018).

[23] T. Matsubara, P. Facchi, V. Giovannetti, and K. Yuasa, Optimal Gaussian metrology for generic multimode interferometric circuit, New J. Phys. **21**, 33014 (2019).

[24] C. Oh, C. Lee, S. H. Lie, and H. Jeong, Optimal distributed quantum sensing using Gaussian states, Phys. Rev. Res. **2**, 023030 (2020).

[25] G. Gramegna, D. Triggiani, P. Facchi, F. A. Narducci, and V. Tamma, Heisenberg scaling precision in multi-mode distributed quantum metrology, arXiv:2003.12550v1.

[26] G. Gramegna, D. Triggiani, P. Facchi, F. A. Narducci, and V. Tamma, Typicality of Heisenberg scaling precision in multi-mode quantum metrology, arXiv:2003.12551v1.

[27] M. R. Grace, C. N. Gagatsos, and S. Guha, Entanglement enhanced estimation of a parameter embedded in multiple phases, arXiv:2004.04152v2.

[28] Q. Zhuang, J. Preskill, and L. Jiang, Distributed quantum sensing enhanced by continuous-variable error correction, New J. Phys. **22**, 022001 (2020).

[29] X. Guo, C. R. Breum, J. Borregaard, S. Izumi, M. V. Larsen, T. Gehring, M. Christandl, J. S. Neergaard-Nielsen, and U. L. Andersen, Distributed quantum sensing in a continuous variable entangled network, Nat. Phys. **16**, 281 (2020).

[30] Y. Xia, W. Li, W. Clark, D. Hart, Q. Zhuang, and Z. Zhang, Demonstration of a Reconfigurable Entangled Radio-Frequency Photonic Sensor Network, Phys. Rev. Lett. **124**, 150502 (2020).

[31] H. Qi, K. Brádler, C. Weedbrook, and S. Guha, Ultimate limit of quantum beam tracking, arXiv:1808.01302.

[32] Q. Zhuang and Z. Zhang, Supervised Learning Enhanced by an Entangled Sensor Network, Phys. Rev. X **9**, 041023 (2019).

[33] H. C. Lefevre, *The Fiber-Optic Gyroscope* (Artech House, Boston, London, 2014), 2nd ed.

[34] H. J. Arditty and H. C. Lefèvre, Sagnac effect in fiber gyroscopes, Opt. Lett. **6**, 401 (1981).

[35] M. J. F. Digonnet and J. N. Chamoun, in *Fiber Optic Sensors and Applications XIII*, edited by E. Udd, G. Pickrell, and H. H. Du, International Society for Optics and Photonics (SPIE, 2016), Vol. 9852, p. 19.

[36] S. W. Lloyd, S. Fan, and M. J. Digonnet, Experimental observation of low noise and low drift in a laser-driven fiber optic gyroscope, J. Lightwave Technol. **31**, 2079 (2013).

[37] S. W. Lloyd, M. J. Digonnet, and S. Fan, Modeling coherent backscattering errors in fiber optic gyroscopes for sources of arbitrary line width, J. Lightwave Technol. **31**, 2070 (2013).

[38] H. A. Haus, K. Bergman, and Y. Lai, Fiber gyro with squeezed radiation, J. Opt. Soc. Am. B **8**, 1952 (1991).

[39] M. Mehmet, T. Eberle, S. Steinlechner, H. Vahlbruch, and R. Schnabel, Demonstration of a quantum-enhanced fiber Sagnac interferometer, Opt. Lett. **35**, 1665 (2010).

[40] R. Stevenson, M. R. Hush, T. Bishop, I. Lesanovsky, and T. Fernholz, Sagnac Interferometry with a Single Atomic Clock, Phys. Rev. Lett. **115**, 163001 (2015).

[41] P. Kok, J. Dunningham, and J. F. Ralph, Role of entanglement in calibrating optical quantum gyroscopes, Phys. Rev. A **95**, 012326 (2017).

[42] C. Luo, J. Huang, X. Zhang, and C. Lee, Heisenberg-limited Sagnac interferometer with multiparticle states, Phys. Rev. A **95**, 023608 (2017).

[43] M. Fink, F. Steinlechner, J. Handsteiner, J. P. Dowling, T. Scheidl, and R. Ursin, Entanglement-enhanced optical gyroscope, New J. Phys. **21**, 53010 (2019).

[44] X. Yu, H. Liang, and X. Wang, Multiple-parameter estimation in a sagnac interferometer, arXiv:1911.02324v1.

[45] C. Xu, L. Zhang, S. Huang, T. Ma, F. Liu, H. Yonezawa, Y. Zhang, and M. Xiao, Sensing and tracking enhanced by quantum squeezing, Photonics Res. **7**, A14 (2019).

[46] H. J. Arditty and H. C. Lefèvre, in *Fiber-Optic Rotation Sensors and Related Technologies* (Springer-Verlag, Berlin, 1982), Chap. 2.1, p. 44.

[47] B. E. A. Saleh and M. C. Teich, *Fundamentals of Photonics* (John Wiley & Sons, Inc., Hoboken, New Jersey, 2007), 2nd ed.

[48] C. C. Cutler, S. A. Newton, and H. J. Shaw, Limitation of rotation sensing by scattering, Opt. Lett. **5**, 488 (1980).